Overcoming Perovskite Corrosion and De-Doping Through Chemical Binding of Halogen Bonds Toward Efficient and Stable Perovskite Solar Cells

Guanhua Ren[1], Wenbin Han[1], Qiang Zhang[1], Zhuowei Li[1], Yanyu Deng[1], Chunyu Liu[1] ✉, Wenbin Guo[1] ✉

HIGHLIGHTS

- Chemical binding of 4-tert-butylpyridine (TBP) is realized through halogen bonds.

- TBP-induced perovskite decomposition and spiro-OMeTAD de-doping are suppressed.

- Modified perovskite solar cells achieve greatly improved efficiency and stability.

ABSTRACT 4-tert-butylpyridine (TBP) is an indispensable additive for the hole transport layer in highly efficient perovskite solar cells (PSCs), while it can induce corrosion decomposition of perovskites and de-doping effect of spiro-OMeTAD, which present huge challenge for the stability of PSCs. Herein, halogen bonds provided by 1,4-diiodotetrafluorobenzene (1,4-DITFB) are employed to bond with TBP, simultaneously preventing perovskite decomposition and eliminating de-doping effect of oxidized spiro-OMeTAD. Various characterizations have proved strong chemical interaction forms between 1,4-DITFB and TBP. With the incorporation of halogen bonds, perovskite film can maintain initial morphology, crystal structure, and light absorbance; meanwhile, the spiro-OMeTAD film shows a relatively stable conductivity with good charge transport property. Accordingly, the device with TBP complex exhibits significantly enhanced stability in

N_2 atmosphere or humidity environment. Furthermore, a champion power conversion efficiency of 23.03% is obtained since perovskite is no longer damaged by TBP during device preparation. This strategy overcomes the shortcomings of TBP in n-i-p PSCs community and enhances the application potential of spiro-OMeTAD in fabricating efficient and stable PSCs.

KEYWORDS 4-tert-butylpyridine; Corrosion; De-doping; Chemical binding; Stability
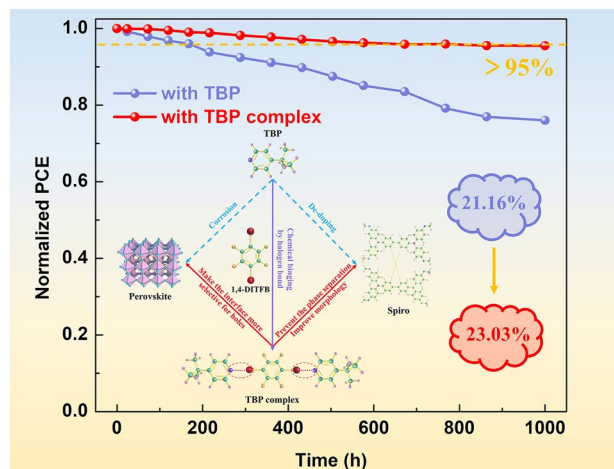
✉ Chunyu Liu, chunyu_liu@jlu.edu.cn; Wenbin Guo, guowb@jlu.edu.cn
[1] State Key Laboratory of Integrated Optoelectronics, College of Electronic Science and Engineering, Jilin University, 2699 Qianjin Street, Changchun 130012, People's Republic of China

1 Introduction

Organic–inorganic hybrid perovskite solar cells (PSCs) have reached a certified record power conversion efficiency (PCE) of 25.7% recently, while the large-scale commercial applications are still limited by the poor stability [1–3]. Numerous efforts have been performed to solve the stability problems caused by water, oxygen, light and heat, as well as the instability of metal oxide/perovskites interface, and several effective strategies have been provided and implemented [4–12]. Everyone knows 2,2′,7,7′-tetrakis-(N,N-di-4-methoxyphenylamino)-9,9′-spirobifluorene (Spiro-OMeTAD, abbreviated as spiro in the following) brings potential risks to stability for n-i-p PSCs [13, 14]. Additives of bis(trifluoromethane) sulfonamide lithium salt (LiTFSI) and 4-tert-butylpyridine (TBP) are needed to enable the device PCE to reach more than 25% at laboratory scale due to lower intrinsic conductivity and hole mobility of pristine spiro [15–18]. Much attention was paid to the device degradation due to the hygroscopicity and Li^+ migration, while the effects of TBP on the stability were rarely addressed and reported at present [19–21].

Actually, TBP has been found to interact with PbI_2, leading to corrosive decomposition of perovskite film [22, 23]. Although the utilization of TBP-LiTFSI complex with the molar ratio of 4:1 can alleviate perovskite corrosion [24], the 6:1 TBP-LiTFSI was more widely applied and the highest device performance is still based on the spiro with more TBP [17]. Moreover, TBP as a nucleophile can react with oxidized spiro (spiro$^+$) to form pyridinated derivatives, which was further confirmed by Lamberti et al. in detail [25–27]. The chemical interaction between TBP and spiro$^+$ induces fast de-doping and reduces the conductivity of hole transport layer (HTL). These two effects will deteriorate the efficiency and long-term stability of PSCs. However, TBP plays an essential role in suppressing photogenerated electron recombination, promoting the dissociation of LiTFSI, preventing the phase separation of HTL, making the interface more selective for holes and so on [27–29]. Though the exact role of TBP is still unclear, it is indispensable for realizing high efficiency PSCs. Introducing the barrier layer fails to completely solve the TBP-induced instability, and this strategy inevitably affects the interface hole transport.

It can be found that the TBP-induced instability arises from reactive activity of pyridine ring [22, 27]. Accordingly,

we conceive to introduce an ideal chemical interaction with pyridine of TBP, thus preventing the further reaction with perovskite and spiro$^+$. Halogen bond has once been established as a crucial interaction in supramolecular chemistry [30], and binding energy of halogen bond is higher than that of regular hydrogen bond [31]. Herein, the 1,4-diiodotetrafluorobenzene (1,4-DITFB) as an ideal halogen bond donor was employed to pre-interact with TBP additive to form complex, since I atoms give strong contacts and F atoms are strong electron-withdrawing groups [32], consequently preventing the corrosion of perovskite film and suppressing the de-doping of spiro$^+$. We systematically characterized and analyzed the film morphology, crystallization, light absorption and photoluminescence (PL) of $FA_{1-x}MA_xPbI_3$ perovskites. The electrical and chemical properties of spiro in solid and solution states have been comprehensively explored as well. Resultantly, PSCs with TBP complex achieve better performance than the devices with TBP in long term and humidity stability tests, as well as a champion PCE of 23.03%.

2 Experimental Section

2.1 Materials

The SnO_2 colloidal dispersion in H_2O (tin (IV) oxide, 15 wt%) was purchased from Alfa Aesar. The lead iodide (PbI_2) ($> 99.99\%$), FAI ($\geq 99.5\%$), MAI ($\geq 99.5\%$), methylammonium chloride (MACl) ($> 99.5\%$), spiro-OMeTAD ($\geq 99.8\%$), LiTFSI ($> 99\%$), TBP ($> 96\%$) and PEAI ($\geq 99.5\%$) were purchased from Xi'an Polymer Light Technology Corp. (China). The 1,4-DITFB (97%) was obtained from Macklin. The N,N-dimethylformamide (DMF, 99.9%) and dimethyl sulfoxide (DMSO, 99%) were obtained from J&K Scientific. The isopropanol (IPA, $\geq 99.7\%$) was purchased from Sinopharm Chemical Reagent Co., Ltd.

2.2 Device Fabrication

The ITO-coated glass substrates were precleaned and treated with UV-zone for 20 min. The SnO_2 precursor was obtained by mixing the SnO_2 colloidal dispersion and deionized water in a volume ratio of 1:4. Then, the SnO_2 precursor was spin coated on the substrate at 3000 rpm for 30 s and

then annealed at 150 °C for 20 min to obtain the SnO_2 electron transport layer. The PbI_2 (1.5 mmol) was dissolved in 1 mL DMF and DMSO (V/V = 9:1), and the solution was spin coated onto the cooled substrate at 2000 rpm for 30 s and then annealed at 70 °C for 1 min. Subsequently, 100 μL of organic mixture solution of (FAI:MAI:MACl = 90 mg:6.39 mg:9 mg in 1 mL IPA) was spin coated onto the PbI_2 film at 2000 rpm for 30 s and annealed at 150 °C for 30 min to form $FA_{1-x}MA_xPbI_3$ perovskite films. The PEAI solution (3 mg mL^{-1} in IPA) was dynamically spin coated on the perovskite at 4000 rpm for 30 s. 1,4-DITFB was dissolved in TBP at different mass fractions (0, 0.5, 1, 2, and 3 wt%). To obtain the spiro solution, 72.3 mg of spiro, 17.6 μL of LiTFSI solution (520 mg mL^{-1} in acetonitrile) and 28.5 μL TBP or 1,4-DITFB-added TBP were dissolved in 1 mL chlorobenzene. Next, the spiro solution was deposited at 4000 rpm for 30 s as the HTL. After that, they are placed in a drying tower for oxidation. Finally, 100-nm thick of Ag electrode was deposited in a vacuum condition ($< 10^{-4}$ pa). The devices were completed, and the effective area is 0.044 cm^2. In the stability tests, 80-nm thick of Au film was deposited in the same way as Ag electrode.

2.3 Characterizations

X-ray diffraction (XRD): The XRD patterns of the perovskite films were measured on a Shimadzu XRD-6000 diffractometer.

Scanning electron microscope (SEM): The cross sectional and surface SEM images were characterized using a JEOL JSM-7500F field-emission SEM.

Atomic force microscope (AFM): The AFM images of the perovskite films and spiro films were obtained with an ICON-PT in tapping mode.

Absorption spectra: The absorption spectra of the perovskite films, spiro films and solutions were performed with UV 1700 photometer, Shimadzu.

Photoluminescence (PL): The PL spectra were conducted on a Shimadzu RF 5301 fluorescence spectrophotometer.

The samples used for the above measurements and shown in Figs. 2d–i and S8-S12 were prepared as the following: We prepared four perovskite films for each measurement. All perovskite films were deposited on the same SnO_2 to maintain consistency with the complete PSCs and exclude the effect of charge transport. The "control" film represents the perovskite film without any treatment; the "with TBP" film represents that we spin-coated the spiro with TBP on the perovskite film and washed it off with CB at the end; the "with TBP complex" film represents that we spin-coated the spiro with TBP complex on the perovskite film and washed it off with CB at the end; the "CB washed" film represents the perovskite film washed with CB for comparison. The amount of CB was 50 μL and washed twice dynamically. Each sample was measured for three different time periods, the first time period is that we placed the samples in the drying tower until the end of the spiro oxidation (the perovskite films without spiro were treated in the same way), the second time period is that we stored the oxidation-completed samples in N_2 for 3 days, and the third time period is that we stored the oxidation-completed samples in N_2 for 7 days. The PL intensities of these samples are based on the "control" film just after oxidation as a standard "1".

Current–voltage (J-V): The J-V curves were measured using a Keithley 2400 source meter under AM 1.5G solar illumination.

X-ray photoelectron spectroscopy (XPS): XPS measurements were conducted on a Thermo Scientific ESCAL-ANTM 250Xi system.

Fourier-transform infrared spectroscopy (FTIR): The FTIR spectra were collected using a Nicolet iS50 FT-IR, and the mass fraction ratio of 1,4-DITFB and TBP was selected 3 wt% for the convenience of analysis.

Electron spin resonance (ESR): The ESR spectra were measured by an electron paramagnetic resonance spectrometer (BRUKER). The samples for ESR spectroscopy measurement were by the method reported in the reference expect that the solvent was changed to chlorobenzene-acetonitrile mixed solvent [27].

Raman: The Raman spectra were measured by a Raman spectrometer (Renishaw) with a laser excitation wavelength of 532 nm. The solid-state samples for Raman spectroscopy measurement were prepared by the method reported in the reference expect that the solvent was changed to chlorobenzene-acetonitrile mixed solvent [27].

Space charge limited current (SCLC): The I-V curves of the samples used for the conductivity and SCLC measurements were obtained by a Keithley 2400 source meter in dark condition.

Incident photon-electron conversion efficiency (IPCE): The IPCE spectra were measured with a Crowntech QTest Station 1000 AD.

Trap density of states (tDOS) and electrochemical impedance spectroscopy (EIS): The tDOS of the PSCs was derived from angle frequency-dependent capacitance (C-F) data. The impedance spectroscopy and C-F curves were characterized using a Precision Impedance Analyzer 6500B Series of Wayne Kerr Electronics.

Transient photovoltage (TPV) and transient photocurrent (TPC): The TPV and TPC measurements were tested using the Keysight DSOX6004A oscilloscope and a nanosecond laser as the light source. The wavelength of light was 532 nm.

Capacitance–voltage (C-V): The *C-V* data were obtained from the TH2829C impedance test.

3 Results and Discussion

3.1 Formation of 1,4-DITFB-TBP Complex

As illustrated in Fig. 1a, TBP results in corrosive decomposition of perovskite and de-doping of spiro, which arises from the pyridine ring. Therefore, halogen bond is introduced to bind TBP and form 1,4-DITFB-TBP complex. The appropriate amount of 1,4-DITFB-TBP complex will not substantially affect the positive effects of TBP, which prevent the phase separation, improve morphology and make the interface more selective for hole. To verify the formation of this complex, XPS of pure 1,4-DIFTB and 1,4-DIFTB-TBP mixture was measured (Fig. 1b–c). The binding energy of I 3*d* shifts to the low binding energy region when adding TBP, and the same phenomenon is observed in the F 1 s XPS spectra, suggesting the increase in electronic state density around I and F atoms. Meanwhile, FTIR is displayed in Figs. 1d–e and S1. Formation of 1,4-DITFB-TBP complex is based on the lone electron pairs of N atoms because the peak of pyridine ring stretching around 1596 cm^{-1} shows a blue-shift, which will prevent the harmful reaction with PbI$_2$ [24, 33]. The peak in the range of 1450–1485 cm^{-1} is the asymmetric vibrations of the tert-butyl group [33], which can be divided it into peak$_M$ and peak$_N$. It is observed that the peak$_M$ position and the ratio of peak area A_M/A_N change, demonstrating that there is indeed an interaction between 1,4-DITFB and TBP. The absorption spectra of pure TBP and 1,4-DITFB-TBP solution are displayed in Fig. 1f. An absorption peak appears at 377 nm for the 1,4-DITFB-TBP solution, which is different from the characteristic peaks of

TBP and 1,4-DITFB [34], thereby proving the generation of 1,4-DITFB-TBP complex. Furthermore, TBP can luminesce under an ultraviolet (UV) lamp irradiation, while such phenomenon is almost invisible with the addition of 1,4-DITFB (Inset of Fig. 1f). The characterizations above qualitatively confirmed that 1,4-DITFB and TBP form the complex by halogen bonds. In subsequent studies, 1,4-DITFB-TBP complex (simply named as TBP complex) is pre-prepared and then added into spiro solution.

3.2 Suppression of Perovskite Decomposition by TBP Complex

Then, we explored the inhibition effect of TBP complex on perovskite decomposition derived from TBP. The detailed corrosion mechanism of TBP on FA$_{1-x}$MA$_x$PbI$_3$ perovskite was obtained from the following phenomena and measurements. It can be found that FA$_{1-x}$MA$_x$PbI$_3$ films were severely corroded by TBP when heating at 85 °C within 5 min compared with the control film at the same temperature (Figs. 2a and S2a). And XRD was carried out to demonstrate the change of perovskite crystal structure (Fig. 2b). The diffraction peaks at 14.14° and 28.26° of α phase perovskite are significantly decreased, while the peak of δ phase perovskite is greatly increased, suggesting that the standard perovskite crystal structure has been badly damaged [35, 36]. The slight shift of diffraction peaks of corroded film may arise from the lattice shrinkage. And PbI$_2$ peak disappears accompanied by the formation of a new diffraction peak (marked with a blue square), indicating the formation of new species. The SEM and AFM measurements also demonstrate that the morphology of this film has been destroyed (Fig. S3). We also observed that perovskite film is seriously corroded at room temperature with 2 μL of TBP in Fig. S2b, indicating that PSCs will inevitably degenerate during device operation and storage even in the present of extremely few TBP in spiro layer. In order to prove TBP in HTL can destroy the perovskite film, SEM images of perovskite without and with spiro layer covering are performed after oxidation, and triple TBP is added into spiro solution to more clearly observe the change of perovskite morphology. Before measurements, perovskite layer covered with spiro layer was washed off twice with 50 μL chlorobenzene (CB) to remove spiro. By comparison, the control film is
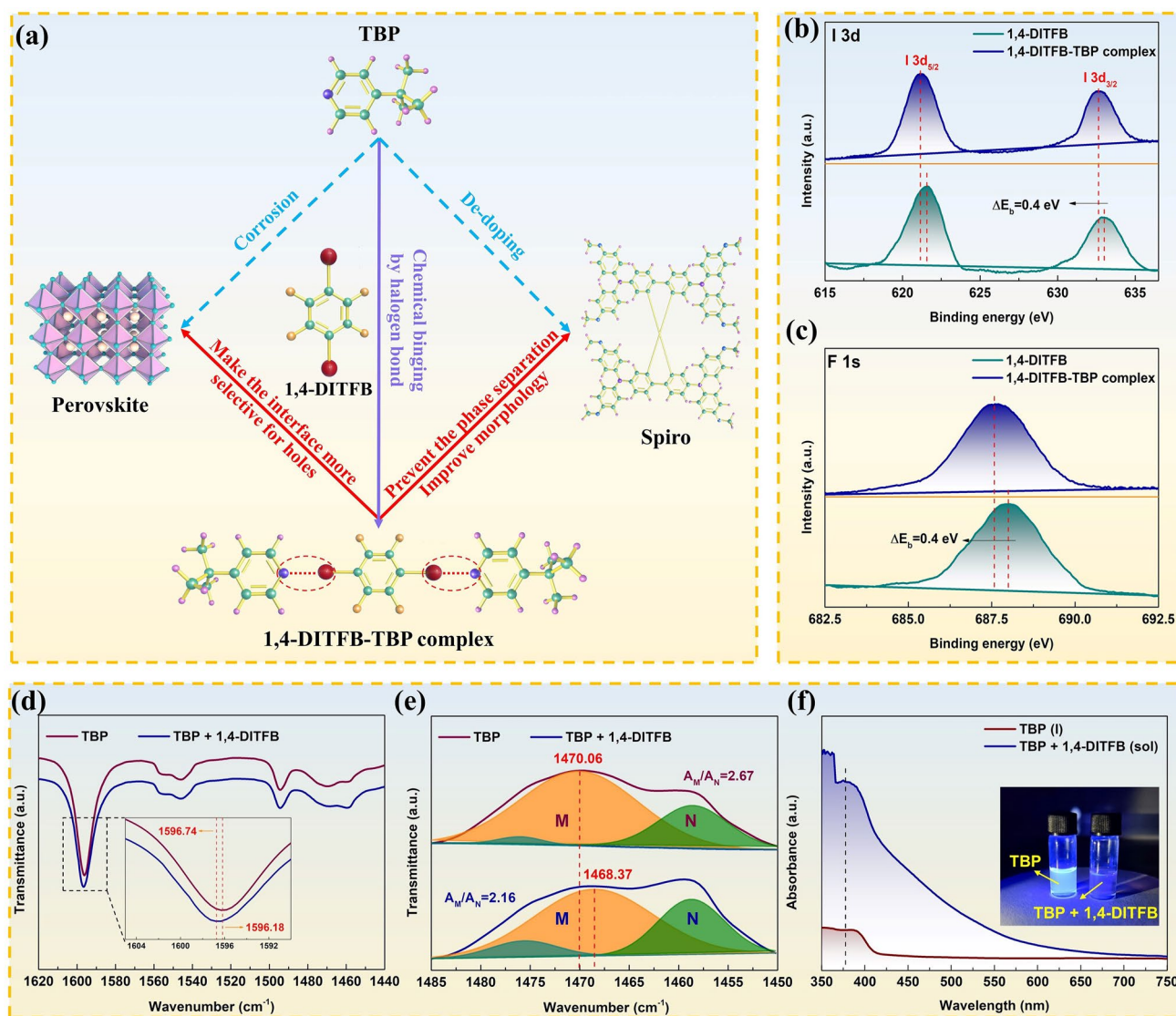
Fig. 1 **a** Schematic illustration of the chemical binding process, and interactions between TBP, 1,4-DITFB-TBP complex, perovskite and spiro. (The red solid arrows show positive effects, while the blue dashed arrows show negative effects.) High-resolution XPS spectra depicting the **b** I 3d and **c** F 1 s peaks of 1,4-DITFB and 1,4-DITFB-TBP complex. FTIR of pure TBP and 1,4-DITFB-TBP solution in the **d** 1440–1620 cm^{-1} and **e** 1450–1485 cm^{-1} range, and the inset is the partial magnification of the spectra. **f** Absorption spectra of pure TBP and 1,4-DITFB-TBP solution. Inset is the optical image of pure TBP and 1,4-DITFB-TBP solution under an UV lamp

also washed by CB. In Fig. S4, the control film exhibits a uniform morphology with grain sizes of 0.5–2.5 µm, while many pits and small particles exist on the surface of perovskite film once covered by spiro, proving the corrosiveness of TBP. Meanwhile, the PSCs based on spiro with triple TBP have poor efficiency and stability (Fig. S5), while the device with triple TBP complex provides the improved efficiency and stability (Fig. S6), and detailed photovoltaic parameters are summarized in Table S1. We

reasonably deduce that the devices with regular TBP still have potential risk to deteriorate with enough time and temperature.

The absorption spectra of pure TBP and PbI$_2$-TBP solution are shown in Fig. 2c. With the addition of PbI$_2$, an absorption peak appears at 407 nm and distinguishes from the characteristic peaks of TBP and PbI$_2$ [37], proving the formation of new species, which can also explain the disappearance of PbI$_2$ peak in Fig. 2b. Pure PbI$_2$ powder and the product obtained by
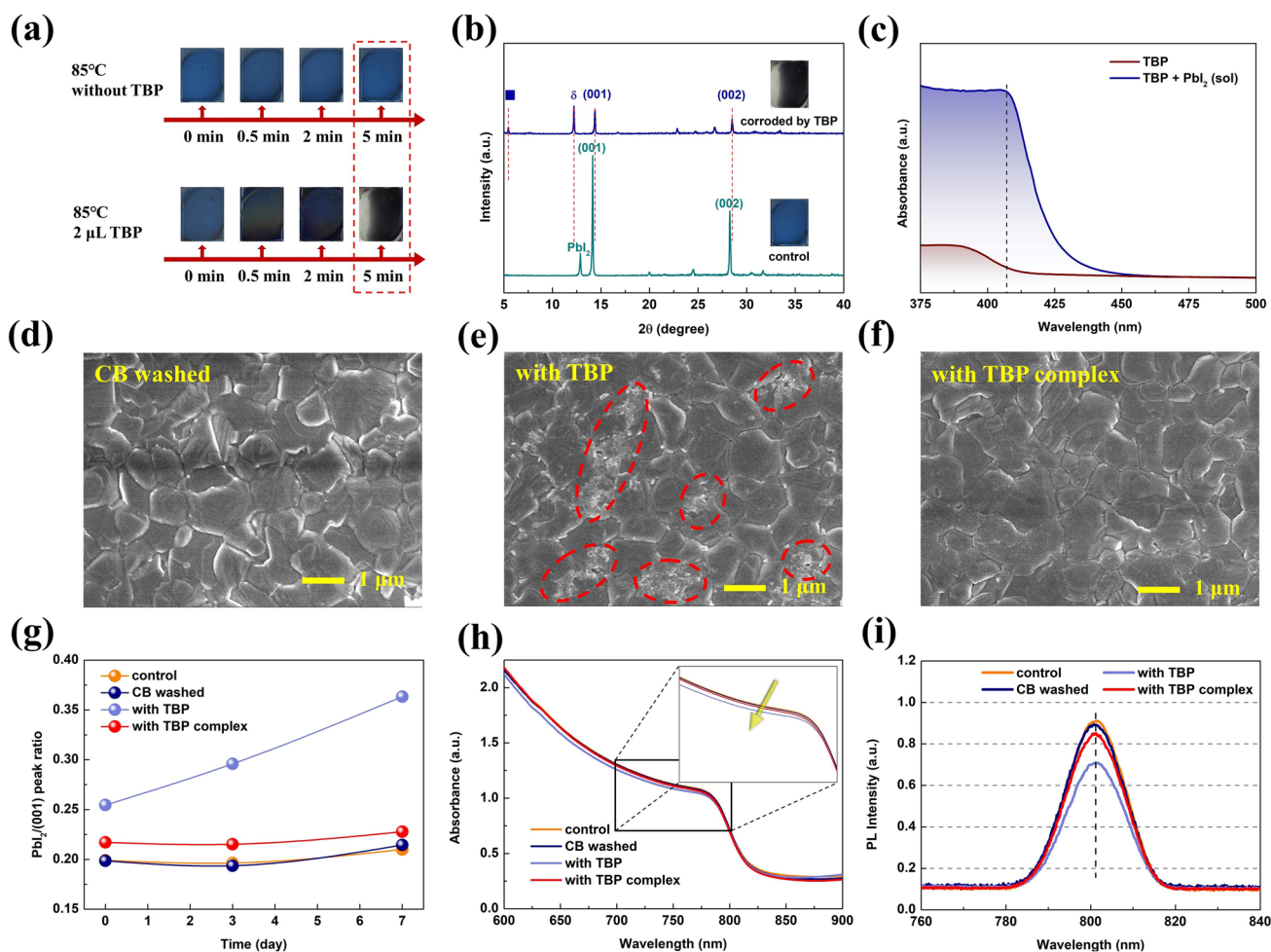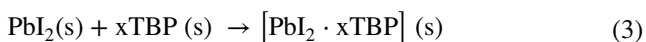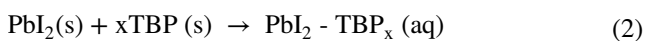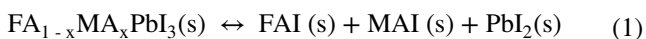
Fig. 2 **a** Photographs of the evolution of $FA_{1-x}MA_xPbI_3$ perovskite films at 85 °C without and with TBP. **b** XRD patterns of the perovskite film corroded by TBP and control film. **c** Absorption spectra of pure TBP and PbI_2-TBP solution. The red dotted line is obtained by subtracting the absorption of pure TBP from the absorption of PbI_2-TBP solution. SEM images of the **d** control film with CB washing, perovskite films once coated with spiro layer with **e** TBP and **f** TBP complex after 7 days of storage in N_2. **g** PbI_2/(001) peak ratio of the films as the function of time. Data are extracted from XRD measurement. Corresponding **h** absorption spectra and **i** steady-state PL spectra. Inset is the partial magnifications of the absorption spectra

drying PbI_2-TBP solution were further characterized by XPS. As illustrated in Fig. S7, the peaks of Pb 4f shift to a lower binding energy after TBP treatment, revealing that TBP interacts with the center Pb to form a complex [38]. Accordingly, the TBP-induced degradation mechanism can be concluded as the following reactions:

$$FA_{1-x}MA_xPbI_3 (s) \leftrightarrow FAI (s) + MAI (s) + PbI_2 (s) \quad (1)$$

$$PbI_2 (s) + xTBP (s) \rightarrow PbI_2 - TBP_x (aq) \quad (2)$$

$$PbI_2 (s) + xTBP (s) \rightarrow [PbI_2 \cdot xTBP] (s) \quad (3)$$

The formation of PbI_2-TBP complex will further induce the perovskite decomposition according to Le Chatelier's principle. With this mechanism, a large number of defects generates on the perovskite surface, which is also the main route of ion migration [39]. The device degradation can be more severe even with advanced sealing techniques.

In view of the mechanism of perovskite degradation, PbI_2 was added to the TBP solution of 1,4-DITFB until saturation, and no precipitation of 1,4-DIFTB was observed, manifesting that PbI_2 could not destroy the chemical reaction between 1,4-DITFB and TBP. Subsequently, we performed a series of measurements on the perovskite films. Figure 2d–f provides the SEM images of

the control film with CB washing, perovskite films once coated with spiro layer with TBP and with TBP complex after 7 days of storage in N_2 (see details in Supporting Information). The films with TBP were seriously corroded (pinholes and small particles appear on the surface), while the perovskite film with TBP complex was essentially unchanged and remained uniform. Even if the perovskite films with spiro layer were stored for 3 day or have just completed oxidation, the obvious morphology damage can be observed (Fig. S8). AFM images are consistent with the SEM results (Fig. S9). The root-mean-square (RMS) roughness of the film with TBP after 7 days is 53.1 nm, much higher than the other three samples.

XRD was utilized to observe the relative changes of characteristic peaks of perovskite and PbI_2. As displayed in Fig. S10, all samples exhibit diffraction peaks of (001), (002), and (111) crystal planes of $FA_{1-x}MA_xPbI_3$ perovskite, accompanied by the PbI_2 peak [35]. The PbI_2/(001) peak ratio as the function of time is shown in Fig. 2g. The reduced ratio for the films with TBP complex demonstrates that the corrosive decomposition of perovskites is mitigated. For corresponding absorption spectra in Figs. 2h and S11, the light absorbance of the perovskite film once covered with spiro doping with TBP complex is higher, and the absorption intensity is relatively stable. The similar trends can be concluded from the difference in PL peak intensity (Figs. 2i and S12). More intuitively, the normalized PL intensity versus time for the samples is extracted into Fig. S12c. The measurements and characterization above have fully proved that TBP can induce perovskite decomposition and destroy crystal quality. The chemical binding from halogen bonds inhibits the reaction of TBP and PbI_2, which successfully mitigates the corrosion effect. Furthermore, we employed AFM and SEM to observe the role of TBP complex on the morphology and microstructure of the spiro film. The spiro film with TBP shows many round-shaped bulges with the RMS roughness of 1.99 nm (Fig. S13b). With TBP complex, the film becomes smooth with the RMS roughness decreased to 1.14 nm (Fig. S13c). It can be attributed that TBP complex slows down the evaporation of TBP, which is a suitable morphology controller as previously described [40, 41]. The SEM images in Fig. S14 indicate that the spiro with TBP complex presents the same surface morphology as the one with TBP.

3.3 Suppression of Spiro De-doping by TBP Complex

Furthermore, the TBP complex is also expected to suppress the TBP-induced spiro de-doping. Figure 3a gives the chemical reactions in spiro layer during oxidation and storage [27]. Spiro+ molecules can increase the HTL conductivity, but the present of TBP reduces its content, which is detrimental to PSCs with FF loss and unexpected charge recombination. We conducted Raman spectroscopy measurement on the different spiro-based samples in the solid state in Fig. S15. The shift of the peak around 732 cm^{-1} toward higher energy confirms that TBP does affect spiro and tends to its amorphous form [27]. The variation of peaks in the range of 1000–1040 cm^{-1} is particularly concerned (Fig. 3b). A peak centered at 1007.5 cm^{-1} is visible for all three samples, which may be the evidence for the mixing of spiro and LiTFSI. The Raman peaks around 1015 and 1027 cm^{-1} were assigned to pyridinium cation species (Py+), while the peak around 1034 cm^{-1} originated from neutral pyridine species (Py), which is labeled in Fig. 3c [42]. Obviously, the Py+ peak disappears for the spiro:LiTFSI:TBP complex powder, suggesting that 1,4-DITFB reduces the generation of Py+. Considering the enhanced molecular diffusion in solution state, the solution samples with the same composition as the powder were also characterized. Interestingly, the solution samples have similar Raman peaks as the powder samples, but the signals of Py+ and Py become intensive, which is beneficial for our analysis (Fig. S16a–b). The peak area ratio of Py+ and Py for spiro:LiTFSI:TBP sample is 0.2619, but the ratio for spiro:LiTFSI:TBP complex sample decreases to 0.1970 (Fig. S16c–d). This is the same as the Raman data of the powder samples.

ESR spectroscopy is an effective tool to detect spiro+ radicals. Lamberti et al. used ESR spectroscopy to explore the de-doping process of spiro in detail [27]. In Fig. S17, the pure spiro sample displays no obvious radical signals. In contrast, the spiro:LiTFSI sample presents strong signals to evidence the existence of spiro+ radicals. The addition of TBP significantly reduces the ESR signal intensity, while the sample with TBP complex gives a stronger signal than the sample with pure TBP. Then, we stored these two samples in dark and N_2 conditions for 7 days. The sample with TBP shows an obvious intensity decrease and shape change (Fig. 3d), which is similar to previous report [27]. The TBP complex can suppress this phenomenon,
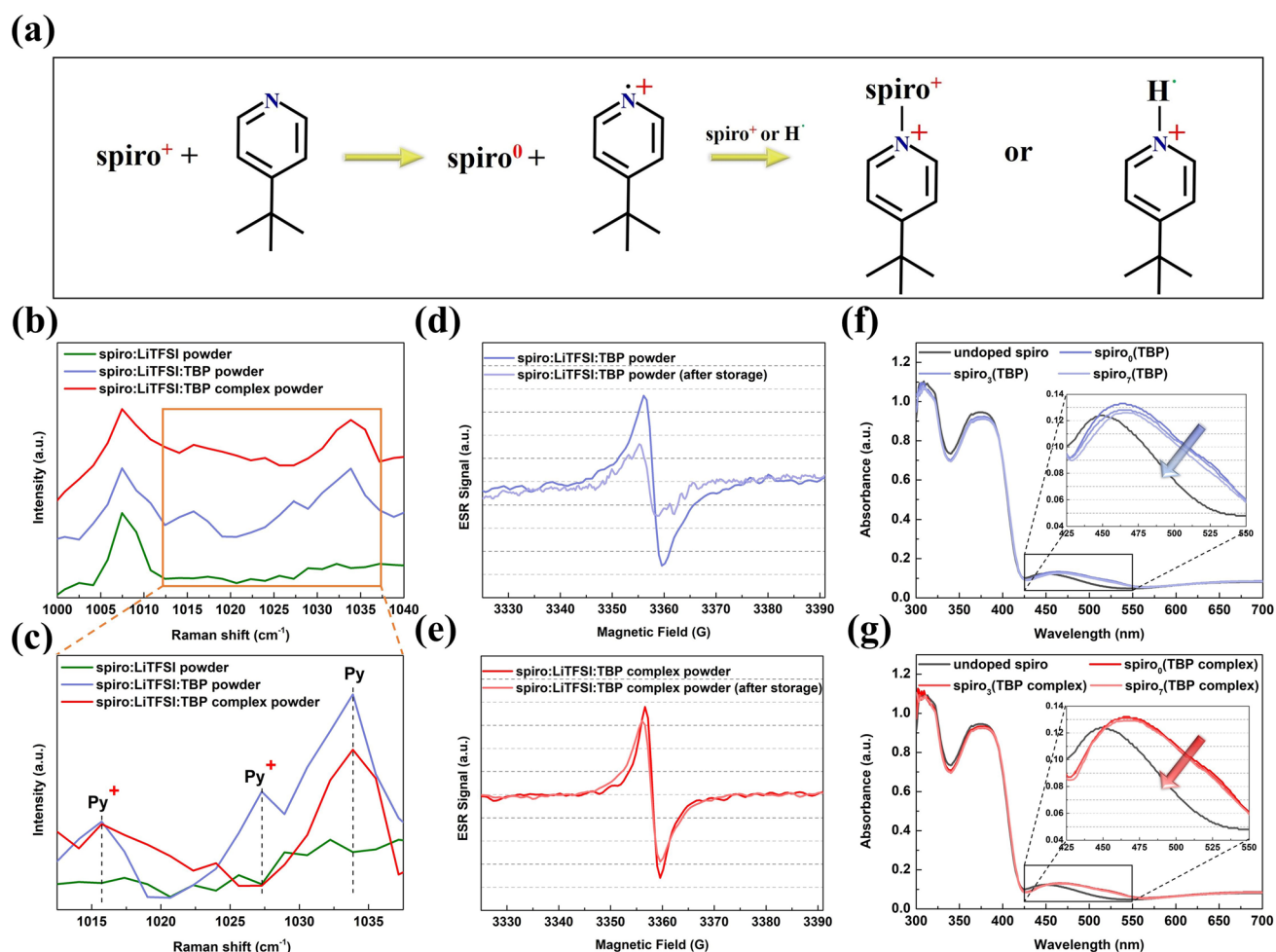
Fig. 3 **a** Reaction mechanism for TBP-induced spiro de-doping. **b** Raman spectra of the different spiro-based powders in the 1000–1040 cm^{-1} range. **c** Magnification of the spectra in the 1012.5–1037.5 cm^{-1}. ESR spectroscopy of the different spiro-based powders with **d** TBP and **e** TBP complex. Absorption spectra of different spiro films with **f** TBP and **g** TBP complex. Insets are the partial magnifications of the spectra

as observed by the mitigated signal attenuation in Fig. 3e. Absorption spectra were used to qualitatively analyze the variation of spiro$^+$ content in spiro films. As exhibited in Fig. 3f–g, the absorption peaks around 523 nm have been assigned to the spiro$^+$ [43]. Tracing the evolution of the peak intensity allows us to observe the increase or decrease of spiro$^+$. The spiro-based films were measured for three time periods and represented by subscripts 0, 3, and 7, respectively. The spiro$^+$ peak of the sample with TBP slightly decreased after storage for 3 and 7 days. In comparison, the peaks of the three samples with TBP complex reveal a negligible difference. The samples in solution state were measured and are illustrated in Fig. S18. Due to the accelerated intermolecular interaction

and possible solvent volatilization, the absorption peak of spiro$^+$ decreases. Similarly, the absorbance of spiro(TBP) is much lower than that of the sample with TBP complex. Subsequently, we measured the electrical conductivity (σ_0) of the spiro films with the device structure of ITO/spiro/Ag (Figs. S19 and S20) [44]. The detailed values are listed in Table S2. The σ_0 of the spiro$_0$(TBP complex) film is 1.75×10^{-5} s cm^{-1}, slightly higher than the spiro$_0$(TBP) film (1.68×10^{-5} s cm^{-1}). After 7 days of storage, the loss of σ_0 is about 13.69% (1.45×10^{-5} s cm^{-1}), but the spiro(TBP complex) film only loses 4.57% of the initial σ_0 (1.67×10^{-5} s cm^{-1}). Figure S21 clarifies that the spiro$_0$(TBP) film and spiro$_0$(TBP complex) film have very similar band structures. The measurements and analysis

prove that the complex reduces the TBP-induced reduction of spiro$^+$ without impairing the film electrical properties, consequently enabling the spiro HTL with better stability.

3.4 Performance and Stability of PSCs

With improved stability of the perovskite layer and spiro HTL, the device performance was subsequently investigated. Device structure is displayed in Fig. 4a, as well as the corresponding cross-sectional SEM image. The concentration of 1,4-DITFB was optimized, and the most suitable concentration was determined to be 2 wt%. Figure S22 and Table S3 show the champion J-V curves and photovoltaic parameters of these PSCs. As summarized in Fig. 4b and Table S4, the device with TBP delivers a high PCE of 21.16%. With TBP complex, the device provides a champion PCE of 23.03%, with a V_{oc} of 1.165 V, a J_{sc} of 24.50 mA cm^{-2}, and a FF of 80.70%. In addition, the hysteresis index (HI) reduces from 4.58 to 1.09% [45]. The enhanced PCE and suppressed hysteresis mainly result from the high quality of the perovskite

and the reduced defects in the device, as well as the slight improvement in spiro layer. And J_{sc} is consistent with the integrated J_{sc} from IPCE spectra in Fig. S23. In Figs. 4c and S24, we can find that the devices with TBP complex demonstrate faster response, indicating more efficient charge extraction than the devices with TBP. Figures 4d and S25 give the distribution of the photovoltaic parameters of 16 individual cells employing the spiro with different contents of 1,4-DITFB.

EIS was commonly performed to study the charge transport and carrier recombination in PSCs [46]. The Nyquist plots measured under illumination and different bias voltages consist of two separate arcs, as exhibited in Figs. 5a and S26. According to the equivalent circuit, it can be seen that the series resistance (R_S) and transfer resistance (R_{tr}) of the device with TBP complex are both lower than those of the device with TBP, while the recombination resistance (R_{rec}) is the opposite. The results at all bias voltages follow the above analysis, clarifying that enhanced hole transport efficiency and reduced carrier recombination are achieved. Halogen bonds can protect perovskites from corrosion decomposition,
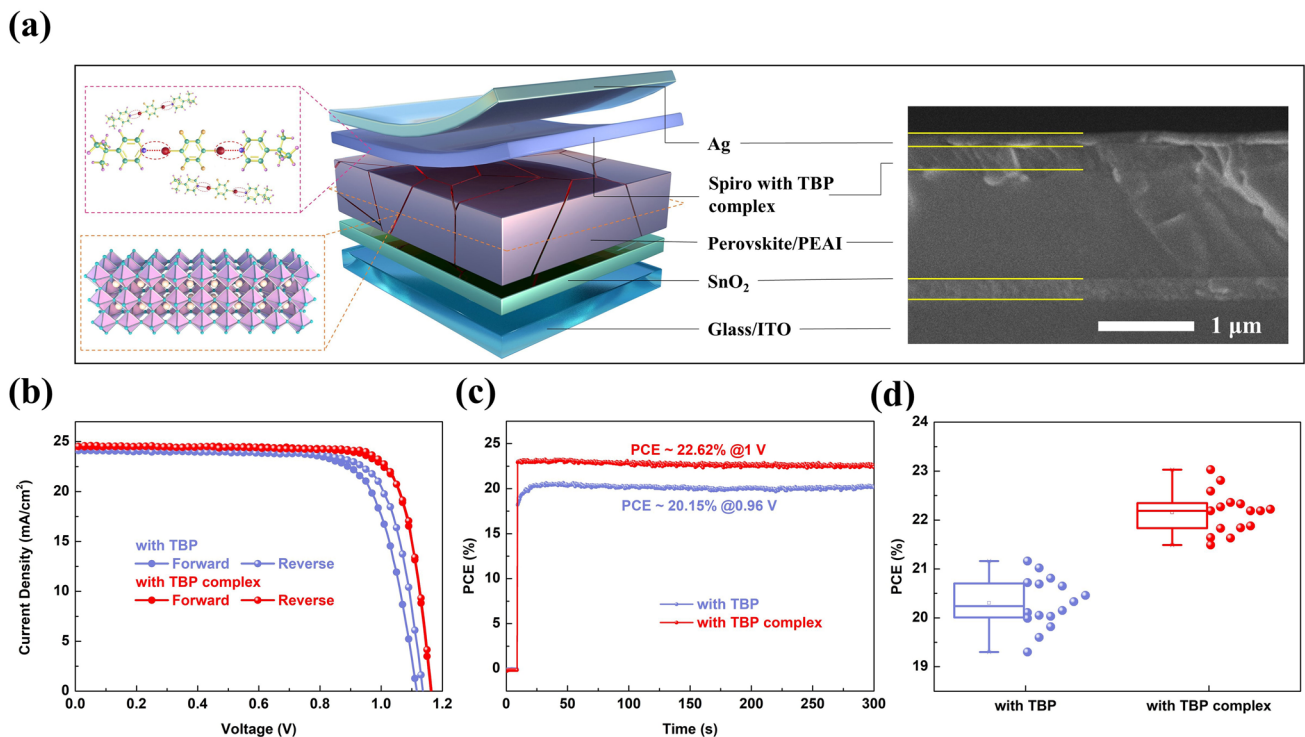

Fig. 4 **a** Structure diagram and corresponding cross-sectional SEM image of fabricated PSCs. **b** J-V curves of the devices with TBP and TBP complex measured by forward and reverse scans. **c** Stabilized PCEs. **d** Distribution of the PCE of the devices with TBP and TBP complex (16 individual cells are included)
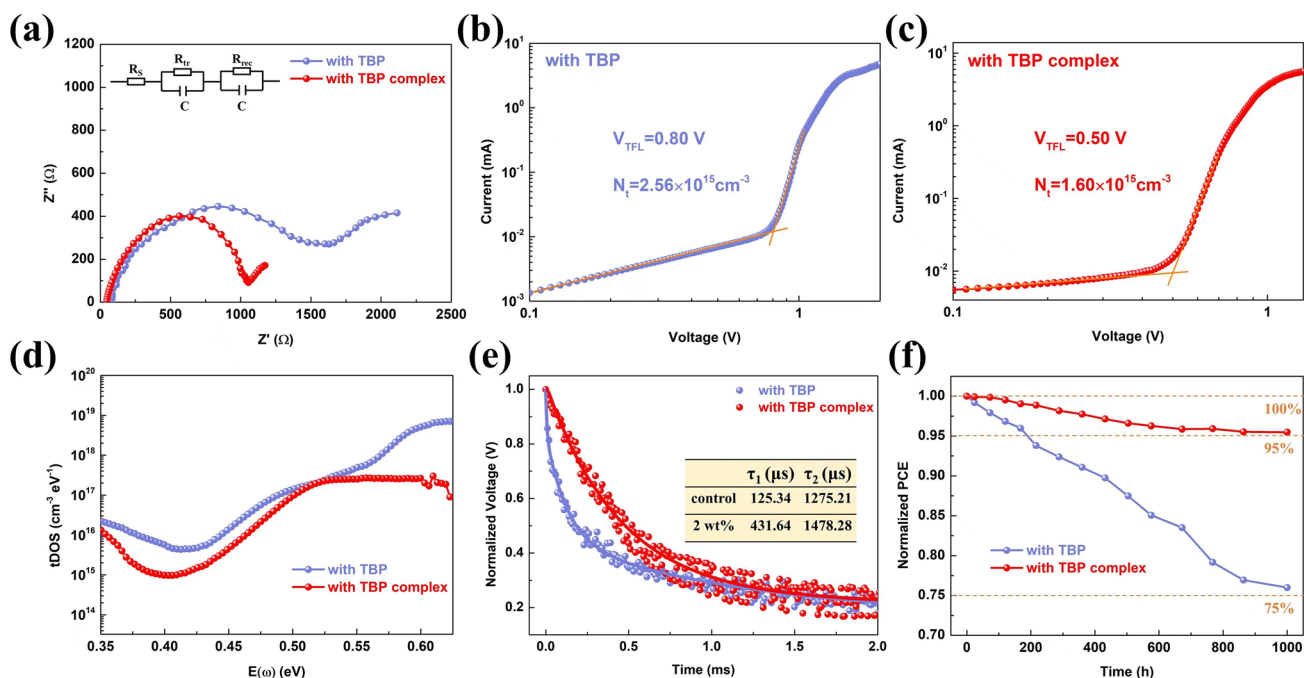
Fig. 5 a Nyquist plots of the devices with TBP and TBP complex measured under 0.8 V bias voltage, and the inset is the equivalent circuit. **b, c** are the *I-V* curves of the hole-only devices with the structure of ITO/PEDOT:PSS/FA$_{1-x}$MA$_x$PbI$_3$/spiro with TBP or TBP complex/Ag. **d** tDOS for the devices with TBP and TBP complex. **e** TPV based on the devices with TBP and TBP complex. **f** PCE evolution of the devices with TBP and TBP complex without encapsulation in N$_2$ atmosphere at room temperature

so as to reduce the formation of defects. Then, the hole-only device with ITO/PEDOT: PSS/FA$_{1-x}$MA$_x$PbI$_3$/spiro/Ag geometry was constructed and the space charge limited current (SCLC) method was used to calculate the trap density (N_t) of perovskite films [47]. With the complex formed through halogen bonds, the N$_t$ of the perovskite film decreased from 2.56×10^{15} to 1.60×10^{15} cm^{-3} (Fig. 5b–c). The thermal admittance spectroscopy measurement was also conducted to analyze the tDOS of the device [48]. As presented in Fig. 5d, the tDOS of the device with TBP complex is reduced compared to the device with TBP. We measured TPV and TPC, and the corresponding curves are presented in Figs. 5e and S27. The device with TBP complex has a higher lifetime for photovoltage and a lower lifetime for photocurrent, revealing the suppressed non-radiative recombination and efficient charge transfer [49]. The curves of 1/C^2-V were plotted to estimate the built-in voltages in Fig. S28. The device with TBP complex has a higher built-in voltage, and therefore, the capacity to separate electrons and holes is better, which is reflected in V_{oc} [50]. Importantly, the PSCs with TBP complex exhibit enhanced stability. In N$_2$ atmosphere and room temperature, the device with TBP

maintains about 75% of its initial PCE, while the PCE only reduces by 5% for the device with TBP complex after 1000 h storage (Figs. 5f and S29). Finally, we tested the humidity stability of the unencapsulated devices. With $40 \pm 5\%$ RH at room temperature, 32% and 10% of their initial PCE are lost for the devices with TBP and with TBP complex after 500 h, respectively (Fig. S30). The stability data at $60 \pm 5\%$ RH and about 85% RH were also measured and are shown in Fig. S31. Compared with the PSCs with TBP, the PSCs with TBP complex exhibit more outstanding stability (89% vs. 65% at $60 \pm 5\%$ RH and 72% vs. 41% at about 85% RH after 240 h).

4 Conclusion

In summary, we developed a chemical binding strategy via halogen bonds to suppress the TBP-induced instability in PSCs. 1,4-DIFTB was applied to interact with the N atom in TBP. After the formation of 1,4-DITFB-TBP complex, the decomposition of perovskites is significantly alleviated, and the de-doping of spiro is suppressed. The

perovskite film with reduced defects and improved crystal quality is achieved. Meanwhile, the spiro HTL well maintained its excellent conductivity, and all of which have been comprehensively proved. As a result, the integrated device with TBP complex achieves a champion PCE of 23.03%. Moreover, the unencapsulated device based on the spiro with TBP complex retains about 95% of its initial PCE after stored for 1000 h in the condition of N_2 and room temperature, as well as excellent humidity stability. This work exemplifies the non-innocent role of TBP as the classic dopant for spiro HTL and raises the possibility for the application of TBP in highly stable PSCs, pushing the step closer to commercialization.

References

1. M.A. Green, E.D. Dunlop, J. Hohl-Ebinger, M. Yoshita, N. Kopidakis et al., Solar cell efficiency tables (version 60). Prog. Photovolt. Res. Appl. **30**(7), 687–701 (2022). https://doi.org/10.1002/pip.3595

2. Y. Rong, Y. Hu, A. Mei, H. Tan, I.S. Makhsud et al., Challenges for commercializing perovskite solar cells. Science **361**(6408), eaat8235 (2018). https://doi.org/10.1126/science.aat8235

3. R. Wang, M. Mujahid, Y. Duan, Z.K. Wang, J. Xue et al., A review of perovskites solar cell stability. Adv. Funct. Mater. **29**(47), 1808843 (2019). https://doi.org/10.1002/adfm.201808843

4. B. Chen, S. Wang, Y. Song, C. Li, F. Hao, A critical review on the moisture stability of halide perovskite films and solar cells. Chem. Eng. J. **430**, 132701 (2022). https://doi.org/10.1016/j.cej.2021.132701

5. S.P. Dunfield, L. Bliss, F. Zhang, J.M. Luther, K. Zhu et al., From defects to degradation: a mechanistic understanding of degradation in perovskite solar cell devices and modules. Adv. Energy Mater. **10**(26), 1904054 (2020). https://doi.org/10.1002/aenm.201904054

6. C.C. Boyd, R. Cheacharoen, T. Leijtens, M.D. McGehee, Understanding degradation mechanisms and improving stability of perovskite photovoltaics. Chem. Rev. **119**(5), 3418–3451 (2019). https://doi.org/10.1021/acs.chemrev.8b00336

7. L.K. Ono, Y. Qi, S. Liu, Progress toward stable lead halide perovskite solar cells. Joule **2**(10), 1961–1990 (2018). https://doi.org/10.1016/j.joule.2018.07.007

8. Y. Sun, X. Fang, Z. Ma, L. Xu, Y. Lu et al., Enhanced UV-light stability of organometal halide perovskite solar cells with interface modification and a UV absorption layer. J. Mater. Chem. C **5**(34), 8682–8687 (2017). https://doi.org/10.1039/C7TC02603J

9. R. Wang, J. Xue, L. Meng, J.W. Lee, Z. Zhao et al., Caffeine improves the performance and thermal stability of perovskite solar cells. Joule **3**(6), 1464–1477 (2019). https://doi.org/10.1016/j.joule.2019.04.005

10. S.H. Li, Z. Xing, B.S. Wu, Z.C. Chen, Y.R. Yao et al., Hybrid fullerene-based electron transport layers improving the thermal stability of perovskite solar cells. ACS Appl. Mater. Interfaces **12**(18), 20733–20740 (2020). https://doi.org/10.1021/acsami.0c02119

11. Y.R. Shi, K.L. Wang, Y.H. Lou, D.B. Zhang, C.H. Chen et al., Unraveling the role of active hydrogen caused by carbonyl groups in surface-defect passivation of perovskite photovoltaics. Nano Energy **97**, 107200 (2022). https://doi.org/10.1016/j.nanoen.2022.107200

12. C.H. Chen, Z.H. Su, Y.H. Lou, Y.J. Yu, K.L. Wang et al., Full-dimensional grain boundary stress release for flexible perovskite indoor photovoltaics. Adv. Mater. **34**(16), 2200320 (2022). https://doi.org/10.1002/adma.202200320

13. G. Ren, W. Han, Y. Deng, W. Wu, Z. Li et al., Strategies of modifying spiro-OMeTAD materials for perovskite solar cells: a review. J. Mater. Chem. A **9**(8), 4589–4625 (2021). https://doi.org/10.1039/D0TA11564A

14. M. Li, Z.K. Wang, Y.G. Yang, Y. Hu, S.L. Feng et al., Copper salts doped spiro-OMeTAD for high-performance perovskite solar cells. Adv. Energy Mater. **6**(21), 1601156 (2016). https://doi.org/10.1002/aenm.201601156

15. D. Poplavskyy, J. Nelson, Nondispersive hole transport in amorphous films of methoxy-spirofluorene-arylamine organic compound. J. Appl. Phys. **93**(1), 341–346 (2002). https://doi.org/10.1063/1.1525866

16. T.H. Schloemer, J.A. Christians, J.M. Luther, A. Sellinger, Doping strategies for small molecule organic hole-transport materials: impacts on perovskite solar cell performance and stability. Chem. Sci. **10**(7), 1904–1935 (2019). https://doi.org/10.1039/C8SC05284K

17. H. Min, D.Y. Lee, J. Kim, G. Kim, K.S. Lee et al., Perovskite solar cells with atomically coherent interlayers on SnO_2 electrodes. Nature **598**(7881), 444–450 (2021). https://doi.org/10.1038/s41586-021-03964-8

18. J.J. Yoo, G. Seo, M.R. Chua, T.G. Park, Y. Lu et al., Efficient perovskite solar cells via improved carrier management. Nature **590**(7847), 587–593 (2021). https://doi.org/10.1038/s41586-021-03285-w

19. I. Lee, J.H. Yun, H.J. Son, T.S. Kim, Accelerated degradation due to weakened adhesion from Li-TFSI additives in perovskite solar cells. ACS Appl. Mater. Interfaces **9**(8), 7029–7035 (2017). https://doi.org/10.1021/acsami.6b14089

20. Z. Li, C. Xiao, Y. Yang, S.P. Harvey, D.H. Kim et al., Extrinsic ion migration in perovskite solar cells. Energy Environ. Sci. **10**(5), 1234–1242 (2017). https://doi.org/10.1039/C7EE00358G

21. L.L. Jiang, Z.K. Wang, M. Li, C.H. Li, P.F. Fang et al., Flower-like MoS_2 nanocrystals: a powerful sorbent of Li^+ in the spiro-OMeTAD layer for highly efficient and stable perovskite solar cells. J. Mater. Chem. A **7**(8), 3655–3663 (2019). https://doi.org/10.1039/C8TA11800K

22. Y. Yue, N. Salim, Y. Wu, X. Yang, A. Islam et al., Enhanced stability of perovskite solar cells through corrosion-free pyridine derivatives in hole-transporting materials. Adv. Mater. **28**(48), 10738–10743 (2016). https://doi.org/10.1002/adma.201602822

23. W. Li, H. Dong, L. Wang, N. Li, X. Guo et al., Montmorillonite as bifunctional buffer layer material for hybrid perovskite solar cells with protection from corrosion and retarding recombination. J. Mater. Chem. A **2**(33), 13587–13592 (2014). https://doi.org/10.1039/C4TA01550A

24. S. Wang, Z. Huang, X. Wang, Y. Li, M. Günther et al., Unveiling the role of tBP-LiTFSI complexes in perovskite solar cells. J. Am. Chem. Soc. **140**(48), 16720–16730 (2018). https://doi.org/10.1021/jacs.8b09809

25. A. Magomedov, E. Kasparavičius, K. Rakstys, S. Paek, N. Gasilova et al., Pyridination of hole transporting material in perovskite solar cells questions the long-term stability. J. Mater. Chem. C **6**(33), 8874–8878 (2018). https://doi.org/10.1039/C8TC02242A

26. E. Kasparavicius, A. Magomedov, T. Malinauskas, V. Getautis, Long-term stability of the oxidized hole-transporting materials used in perovskite solar cells. Chem. A Eur. J. **24**(39), 9910–9918 (2018). https://doi.org/10.1002/chem.201801441

27. F. Lamberti, T. Gatti, E. Cescon, R. Sorrentino, A. Rizzo et al., Evidence of spiro-OMeTAD de-doping by tert-butylpyridine additive in hole-transporting layers for perovskite solar cells. Chem **5**(7), 1806–1817 (2019). https://doi.org/10.1016/j.chempr.2019.04.003

28. E.J. Juarez-Perez, M.R. Leyden, S. Wang, L.K. Ono, Z. Hawash et al., Role of the dopants on the morphological and transport properties of spiro-MeOTAD hole transport layer. Chem. Mater. **28**(16), 5702–5709 (2016). https://doi.org/10.1021/acs.chemmater.6b01777

29. S.N. Habisreutinger, N.K. Noel, H.J. Snaith, R.J. Nicholas, Investigating the role of 4-tert butylpyridine in perovskite solar cells. Adv. Energy Mater. **7**(1), 1601079 (2017). https://doi.org/10.1002/aenm.201601079

30. G. Cavallo, P. Metrangolo, R. Milani, T. Pilati, A. Priimagi et al., The halogen bond. Chem. Rev. **116**(4), 2478–2601 (2016). https://doi.org/10.1021/acs.chemrev.5b00484

31. P. Metrangolo, G. Resnati, Halogen versus hydrogen. Science **321**(5891), 918–919 (2008). https://doi.org/10.1126/science.1162215

32. I.G. Grosu, L. Pop, M. Miclăuş, N.D. Hădade, A. Terec et al., Halogen bonds (N--I) at work: supramolecular catemeric architectures of 2,7-dipyridylfluorene with ortho-, meta-, or para-diiodotetrafluorobenzene isomers. Cryst. Growth Des. **20**(5), 3429–3441 (2020). https://doi.org/10.1021/acs.cgd.0c00205

33. S. Yurdakul, M. Bahat, Fourier transform infrared and Raman spectroscopic studies on 4-tert.butylpyridine and its metal(II) tetracyanonickelate complexes. J. Mol. Struct. **412**(1), 97–102 (1997). https://doi.org/10.1016/S0022-2860(96)09392-1

34. H. Sun, M. Wang, A. Khan, Y. Shan, K. Zhao et al., Co-crystals with delayed fluorescence assembled by 1,4-diiodotetrafluorobenzene and polycyclic aromatic compounds via halogen bonds. ChemistrySelect **2**(22), 6323–6330 (2017). https://doi.org/10.1002/slct.201701288

35. F.Z. Qiu, M.H. Li, S. Wang, J.Y. Sun, Y. Jiang et al., Regulating the crystalline phase of intermediate films enables $FA_{1-x}MA_xPbI_3$ perovskite solar cells with efficiency over 22%. J. Mater. Chem. A **9**(42), 24064–24070 (2021). https://doi.org/10.1039/D1TA06410J

36. F. Ma, J. Li, W. Li, N. Lin, L. Wang et al., Stable α/δ phase junction of formamidinium lead iodide perovskites for enhanced near-infrared emission. Chem. Sci. **8**(1), 800–805 (2017). https://doi.org/10.1039/C6SC03542F

37. A.F. Silva, N. Veissid, C.Y. An, I. Pepe, N.B. Oliveira et al., Optical determination of the direct bandgap energy of lead iodide crystals. Appl. Phys. Lett. **69**(13), 1930–1932 (1996). https://doi.org/10.1063/1.117625

38. S. Chen, R. Pei, T. Zhao, D.J. Dyer, Gold nanoparticle assemblies by metal ion-pyridine complexation and their rectified quantized charging in aqueous solutions. J. Phys. Chem. B **106**(8), 1903–1908 (2002). https://doi.org/10.1021/jp013574e

39. L.K. Ono, S. Liu, Y. Qi, Reducing detrimental defects for high-performance metal halide perovskite solar cells. Angew. Chem. Int. Ed. **59**(17), 6676–6698 (2020). https://doi.org/10.1002/anie.201905521

40. Y. Liu, Y. Hu, X. Zhang, P. Zeng, F. Li et al., Inhibited aggregation of lithium salt in spiro-OMeTAD toward highly efficient perovskite solar cells. Nano Energy **70**, 104483 (2020). https://doi.org/10.1016/j.nanoen.2020.104483

41. N.D. Pham, J. Shang, Y. Yang, M.T. Hoang, V.T. Tiong et al., Alkaline-earth bis(trifluoromethanesulfonimide) additives for

efficient and stable perovskite solar cells. Nano Energy **69**, 104412 (2020). https://doi.org/10.1016/j.nanoen.2019.104412

42. D.J. Rogers, S.D. Luck, D.E. Irish, D.A. Guzonas, G.F. Atkinson, Surface enhanced Raman spectroscopy of pyridine, pyridinium ions and chloride ions adsorbed on the silver electrode. J. Electroanal. Chem. Interfacial Electrochem. **167**(1), 237–249 (1984). https://doi.org/10.1016/0368-1874(84)87069-0

43. J. Zhang, Q. Daniel, T. Zhang, X. Wen, B. Xu et al., Chemical dopant engineering in hole transport layers for efficient perovskite solar cells: insight into the interfacial recombination. ACS Nano **12**(10), 10452–10462 (2018). https://doi.org/10.1021/acsnano.8b06062

44. G. Ren, Z. Li, W. Wu, S. Han, C. Liu et al., Performance improvement of planar perovskite solar cells with cobalt-doped interface layer. Appl. Surf. Sci. **507**, 145081 (2020). https://doi.org/10.1016/j.apsusc.2019.145081

45. Q. Xiong, C. Wang, Q. Zhou, L. Wang, X. Wang et al., Rear interface engineering to suppress migration of iodide ions for efficient perovskite solar cells with minimized hysteresis. Adv. Funct. Mater. **32**(7), 2107823 (2022). https://doi.org/10.1002/adfm.202107823

46. P. Yadav, M.H. Alotaibi, N. Arora, M.I. Dar, S.M. Zakeeruddin et al., Influence of the nature of a cation on dynamics of charge transfer processes in perovskite solar cells. Adv. Funct. Mater. **28**(8), 1706073 (2018). https://doi.org/10.1002/adfm.201706073

47. S. Yuan, Y. Xian, Y. Long, A. Cabot, W. Li et al., Chromium-based metal-organic framework as a-site cation in $CsPbI_2Br$ perovskite solar cells. Adv. Funct. Mater. **31**(51), 2106233 (2021). https://doi.org/10.1002/adfm.202106233

48. C. Liu, D. Zhang, Z. Li, X. Zhang, L. Shen et al., Efficient 4,4′,4″-tris(3-methylphenylphenylamino)triphenylamine (m-MTDATA) hole transport layer in perovskite solar cells enabled by using the nonstoichiometric precursors. Adv. Funct. Mater. **28**(36), 1803126 (2018). https://doi.org/10.1002/adfm.201803126

49. Z. Xiong, X. Chen, B. Zhang, G.O. Odunmbaku, Z. Ou et al., Simultaneous interfacial modification and crystallization control by biguanide hydrochloride for stable perovskite solar cells with PCE of 24.4%. Adv. Mater. **34**(8), 2106118 (2022). https://doi.org/10.1002/adma.202106118

50. J. Zhang, Y. Fang, W. Zhao, R. Han, J. Wen et al., Molten-salt-assisted $CsPbI_3$ perovskite crystallization for nearly 20%-efficiency solar cells. Adv. Mater. **33**(45), 2103770 (2021). https://doi.org/10.1002/adma.202103770